

# Predictions of Thermal and Gravitational Signals of Jupiter's Deep Zonal Winds

JUNJUN LIU\*, TAPIO SCHNEIDER

*California Institute of Technology, Pasadena, California, USA*

YOHAI KASPI

*Weizmann Institute of Science, Rehovot, Israel*

(1 March 2012)

## ABSTRACT

NASA's Juno spacecraft will make microwave and gravity measurements of Jupiter. These can reveal information about the composition of Jupiter's atmosphere and about the temperature and density structure below the visible clouds, which is in balance with the structure of the zonal winds. Here we show that there exist strong physical constraints on the structure of the deep zonal winds, and that these imply dynamical constraints on the thermal and gravitational signals Juno will measure. The constraints derive from the facts that Jupiter is rapidly rotating, has strong intrinsic heat fluxes emanating from the deep interior, and has nearly inviscid flow. Because of the strong intrinsic heat fluxes, Jupiter's interior is convecting, but the rapid rotation and weak viscosity constrain the convective motions to occur primarily along cylinders parallel to the planet's spin axis. Convection is expected to approximately homogenize entropy along the spin axis and adjust the interior to a convectively and inertially nearly neutral state. Additionally, thermal wind balance relates entropy gradients perpendicular to the spin axis to the zonal wind shear between the observed cloud-level winds and winds in the deep interior (pressures of order  $10^6$  bar), which must be much weaker because otherwise the Ohmic energy dissipation produced by the interaction of the zonal winds with the planetary magnetic field would exceed the planetary luminosity. Combining these physical constraints with thermal and electrical properties of the atmosphere, we obtain that zonal winds likely extend deeply into Jupiter (to a depth between  $0.84R_J$  and  $0.94R_J$  with Jupiter radius  $R_J$ ) but have strengths similar to cloud level winds only within the outer few percent of Jupiter's radius. Meridional equator-to-pole temperature contrasts in thermal wind balance with the zonal winds increase with depth and reach  $\sim 1-2$  K at 50 bar; they would reach  $O(10$  K) if the winds were shallowly confined, as has been proposed previously. Such temperature contrasts will be detectable by Juno's microwave instrument. The associated gravitational signals of the zonal winds will also be detectable by Juno, but they will be more difficult to distinguish from those implied by flow models that have been proposed previously.

## 1. Introduction

The only available data about the zonal wind, temperature, and density of Jupiter below the visible clouds come from the descent of the Galileo probe into the planet in 1995, delivering data about the atmosphere at the entry point ( $6.5^\circ\text{N}$ ) up to pressures of  $\sim 21$  bar (Atkinson et al. 1997, 1998). NASA's Juno mission will reach Jupiter in 2016 and is expected to deliver the first global data of the temperature and density structure below the visible clouds. It will make microwave and gravity measurements from orbit around Jupiter. These measurements will contain information about the composition of the atmosphere (which affects emissivities and the equation of state) and about the flow (which affects temperature and density gradients). To disentangle compositional and dynamical information, it is essential to have independent constraints on either. Here we show

that there exist strong dynamical constraints on the density and temperature structure, and we calculate the gravity and temperature signals they imply under plausible assumptions for free parameters in the flow structure.

The dynamical constraints derive from the well known facts that Jupiter is rapidly rotating, has strong intrinsic heat fluxes emanating from the deep interior, and has nearly inviscid flow (Ingersoll et al. 2004; Guillot et al. 2004). The intrinsic heat flux ( $\sim 6 \text{ W m}^{-2}$ ) is sufficiently strong to lead to convection in Jupiter's deep interior, up to near the tropopause (Guillot 1999). Convective plumes penetrating into the upper troposphere have indeed been observed (Gierasch et al. 2000; Porco et al. 2003; Sánchez-Lavega et al. 2008). Jupiter's rapid planetary rotation (small Rossby numbers) and negligible viscosity imply that convective motions are predominantly confined to surfaces of constant angular momentum per unit mass (Busse 1976, 1994; Kaspi et al. 2009). These angular momentum surfaces are approximately cylinders concentric with the planet's spin axis

---

\*Corresponding author address: Junjun Liu, California Institute of Technology, Mail Code 131-24, 1200 E. California Blvd., Pasadena, CA 91125. E-mail: ljj@gps.caltech.edu

because the small Rossby number means the angular momentum is dominated by the contribution from the planetary rotation. Because viscous dissipation is negligible in Jupiter's atmosphere and radiative adjustment timescales below the upper troposphere are longer than convective timescales (Guillot et al. 2004; Guillot 2005), we expect that, in the interior, entropy is approximately materially conserved in convective motions and so will become approximately homogenized along angular momentum surfaces. That is, we expect that convection homogenizes entropy in the direction of the planet's spin axis, but not necessarily perpendicular to it (Liu and Schneider 2010), establishing a state that is nearly neutral with respect to convective and inertial instabilities, in which entropy and angular momentum surfaces are aligned (Emanuel 1983; Thorpe and Rotunno 1989; Emanuel 1994). Indeed, data from the descent of the Galileo probe show that the stratification of the atmosphere below the clouds is close to convectively neutral (Magalhães et al. 2002).

Entropy gradients perpendicular to the spin axis are not constrained by convection but are related to the zonal wind and its shear through thermal wind balance (Kaspi et al. 2009). The zonal wind shear below the visible clouds is not generally known (except in the upper layers of the atmosphere and at the Galileo entry site); however, the zonal wind at the cloud level is known (Porco et al. 2003). It is very unlikely that the zonal winds extend into the deep interior unabatedly because if they would, their interaction with the planetary magnetic field would generate electric currents deep in the interior, where the atmosphere is electrically conducting (Nellis et al. 1996). The Ohmic energy dissipation of these electric currents (and thus ultimately the dissipation of kinetic energy) would exceed the net planetary luminosity (Liu et al. 2008). This is impossible since the kinetic energy dissipation cannot exceed the total energy available to drive the flow from intrinsic heat fluxes and absorption of solar energy combined. Liu et al. (2008) showed that at  $0.96R_J$  (Jupiter radius  $R_J$ ), the zonal winds must be weaker than the observed upper-tropospheric winds for the Ohmic dissipation to be smaller than the net planetary luminosity. Further evidence of the weak zonal winds in Jupiter's interior comes from the secular variation of Jupiter's magnetic field, which suggests flow velocities of order of  $10^{-3} \text{ m s}^{-1}$  in the planetary interior (Russell et al. 2001; Guillot et al. 2004). So the zonal wind shear is constrained by observations of the winds at cloud level and the requirement that at some imprecisely known depth the winds are negligibly weak compared with the cloud-level winds. We will exploit these constraints and combine them with thermal wind balance to make predictions of the thermal and gravitational signals

of Jupiter's deep zonal winds, assuming a fixed composition (equation of state) of the atmosphere.

Section 2 begins with a review of thermal wind balance in a deep atmosphere and calculates the temperature structure implied by the zonal winds, under different assumptions about the level at which they are negligibly weak. Section 3 calculates the gravitational signals implied by the zonal winds. Section 4 summarizes the results and implications for measurements by the Juno mission.

## 2. Thermal signals of deep zonal winds

### a. Thermal wind balance in a deep atmosphere

Jupiter's rapid rotation means that the Rossby number  $Ro = U/(2\Omega L_\perp)$  is small (with zonal velocity scale  $U$ , angular velocity of planetary rotation  $\Omega$ , and length scale of zonal-flow variations  $L_\perp$  in the direction perpendicular to the planet's spin axis). With typical scales for upper-tropospheric zonal winds ( $U \lesssim 100 \text{ m s}^{-1}$ ,  $L_\perp \sim 2000 \text{ km}$ ), the Rossby number is  $\lesssim 0.1$ , and it is even smaller for the weaker zonal winds expected in the planetary interior (Schneider and Liu 2009). Additionally, viscous and other momentum dissipation is expected to be weak (small Ekman number) above any dissipative layer at depth. Therefore, the atmospheric flow above any dissipative layer at depth is expected to be in geostrophic balance to leading order, and to the extent the atmosphere is also in hydrostatic balance, thermal wind balance holds. For a deep atmosphere (i.e., not making the thin-shell approximation), the thermal wind balance in the anelastic approximation is (Kaspi et al. 2009)

$$2\boldsymbol{\Omega} \cdot \nabla \mathbf{u} - 2\boldsymbol{\Omega} \nabla \cdot \mathbf{u} = \alpha_s \nabla s' \times \mathbf{g}. \quad (1)$$

Here,  $\boldsymbol{\Omega}$  is the planetary angular velocity vector,  $\mathbf{u}$  is the 3D atmospheric velocity vector,  $\mathbf{g}(r)$  is the gravitational acceleration, and  $s$  is the specific entropy; primes denote fluctuations about a reference state with constant entropy  $\tilde{s}$  and with hydrostatically balanced pressure  $\tilde{p}(r)$  and density  $\tilde{\rho}(r)$

$$\nabla \tilde{p}(r) = \tilde{\rho}(r) \mathbf{g}(r), \quad (2)$$

where  $r$  is the spherical radius. (We neglect Jupiter's oblateness throughout this paper. The gravitational acceleration  $\mathbf{g}(r)$  depends on the density  $\tilde{\rho}(r)$  in the hydrostatic reference state and varies with  $r$ .) The coefficient

$$\alpha_s = -\frac{1}{\tilde{\rho}} \left( \frac{\partial \rho}{\partial s} \right)_p \quad (3)$$

is an entropic expansion coefficient that relates isobaric density fluctuations to entropy fluctuations (i.e.,  $\rho'/\tilde{\rho} =$

$-\alpha_s s'$  at  $p' = 0$ ); for an ideal gas,  $\alpha_s = 1/c_p$ , where  $c_p$  is the specific heat capacity at constant pressure.

For our purposes, it is convenient to use cylindrical coordinates (with cylindrical radius  $r_\perp$  and height  $z$  above the equatorial plane measured in the direction of the planet's spin axis), and to focus on the zonal (azimuthal) wind component  $u$ . Thermal wind balance then becomes<sup>1</sup>

$$2\Omega \frac{\partial u}{\partial z} = \alpha_s g \sin \phi \frac{\partial s'}{\partial r_\perp} - \alpha_s g \cos \phi \frac{\partial s'}{\partial z}, \quad (5)$$

where  $\phi$  is latitude, related to the cylindrical coordinates through

$$\sin \phi(z, r_\perp) = \frac{z}{(z^2 + r_\perp^2)^{1/2}}. \quad (6)$$

A strong intrinsic heat flux emanates from deep inside Jupiter and leads to convection in Jupiter's interior. This convection is expected to be sufficiently vigorous to homogenize entropy along the direction of convective motions (Guillot and Morel 1995; Guillot 2005). Because the Rossby number is small and viscous momentum dissipation and thermal diffusion are negligible, convective motions are approximately aligned with surfaces of constant planetary angular momentum, which are cylinders concentric with the planet's spin axis (Busse 1976; Kaspi et al. 2009). Therefore, where solar radiative fluxes are sufficiently weak and thermal radiative opacities and hence radiative adjustment timescales are sufficiently large (below the upper troposphere), convection tends to homogenize entropy in the direction of the planet's spin axis. The radiative-convective equilibrium state with entropy homogenized along angular momentum surfaces is neutral with respect to convective and inertial axisymmetric instabilities and has zero slantwise convective available potential energy, which convection tends to deplete (Emanuel 1994; Thorpe and Rotunno 1989). The tendency of convection to homogenize entropy in the direction of the spin axis ( $\partial s'/\partial z \approx 0$ ) means that the thermal wind balance (5), where radiative influences are sufficiently weak, reduces to

$$\frac{\partial u}{\partial z} \approx \frac{\alpha_s g \sin \phi(z, r_\perp)}{2\Omega} \frac{\partial s'}{\partial r_\perp}. \quad (7)$$

<sup>1</sup>This thermal wind equation reduces to the standard thermal wind equation for an ideal-gas atmosphere ( $s' = c_p \log \theta$  with potential temperature  $\theta$ ) in the limit of a thin atmospheric shell ( $r = a = \text{const}$ , neglecting vertical Coriolis accelerations),

$$\frac{\partial u}{\partial \tilde{z}} = -\frac{g}{f\theta} \frac{\partial \theta}{\partial y}. \quad (4)$$

Here,  $y = a\phi$  is the meridional coordinate,  $\tilde{z}$  is the altitude (spherical radius) coordinate (with  $\tilde{z} \sin \phi = z$  and  $\tilde{z} \cos \phi = r_\perp$ ), and  $f = 2\Omega \sin \phi$  is the Coriolis parameter.

This relates entropy gradients perpendicular to the spin axis to the zonal velocity shear along the spin axis. Evidence that this is in fact the dominant balance comes, for example, from the general circulation model simulations of Jupiter's upper atmosphere in Schneider and Liu (2009) and Liu and Schneider (2010), which have radiative and intrinsic energy fluxes consistent with Jupiter observations and equilibrate to a statistically steady state with entropy approximately homogenized along angular momentum surfaces below  $\sim 0.7$  bar and away from the equator. At deeper levels in the simulations and away from the equator, the meridional entropy gradient (the thin-shell analog of  $\partial s'/\partial r_\perp$ ) varies with latitude, and the vertical entropy gradient is about an order of magnitude smaller than the meridional entropy gradient. (Within a few degrees of the equator, this is not necessarily true, as the Rossby number may not be small; however, our focus here is on the off-equatorial regions.)

#### b. Constraints on the depth of zonal winds and on entropy gradients

The thermal wind balance (7) shows how a given zonal wind shear along the spin axis is associated with an entropy gradient perpendicular to the spin axis. The zonal wind shear is related to the penetration depth of substantial zonal winds. If the zonal winds are confined to a shallow weather layer (e.g., Ingersoll et al. 2004), the zonal wind shear along the spin axis and the associated entropy gradient perpendicular to it are large. If the zonal winds penetrate deeply (e.g., Busse 1994), the zonal wind shear along the spin axis and the associated entropy gradient perpendicular to it are smaller.

Within the atmospheric shell with substantial zonal winds, the zonal winds are almost certainly sheared in the direction of the spin axis, and the associated entropy gradients perpendicular to the spin axis are nonzero. The reason is that the zonal winds and entropy gradients must satisfy two constraints: (i) they must be approximately in thermal wind balance where dissipation is weak; (ii) along any angular momentum surface (approximately a cylinder), the net angular momentum flux convergence by eddies must be balanced by angular momentum dissipation at depth (Schneider and Liu 2009; Liu and Schneider 2010). These twin constraints generally cannot be satisfied with zonal winds that do not vary in the direction of the spin axis. Rather, zonal winds generally must be sheared along angular momentum surfaces, as seen in the simulations in Schneider and Liu (2009) and Kaspi et al. (2009) and at the Galileo entry site on Jupiter (Magalhães et al. 2002). The Taylor-Proudman state, in which entropy is completely homogenized and the zonal winds are constant along the spin

axis, is unlikely to be attained in the atmospheric shell of substantial zonal winds.

For Jupiter, observations of the flow in the upper troposphere provide constraints on the depth to which substantial zonal winds can extend. It has been observed that in the upper troposphere, eddies generally transport angular momentum out of retrograde and into prograde jets, thus transferring kinetic energy to the mean zonal winds (Ingersoll et al. 1981; Salyk et al. 2006). It is not clear how deeply into the atmosphere this kinetic energy transfer extends. But if the eddy angular momentum fluxes per unit volume extended unabatedly over a layer of only 50 km thickness (e.g., from about 0.3 to 2.5 bar pressure) and if vertical zonal-wind variations over this layer are weak (as is generally assumed), the total energy conversion rate would already amount to  $0.5 \text{ W m}^{-2}$ , or  $\sim 4\%$  of the total energy uptake of the atmosphere from intrinsic heat fluxes and absorption of solar radiation. It would be correspondingly larger or smaller if the angular momentum fluxes were confined to a deeper or shallower layer (Liu and Schneider 2010). The implication is that, in a statistically steady state, mean-flow kinetic energy must either be dissipated at depth at a rate equal to the upper-tropospheric transfer from eddies or must be transferred back to eddies by angular momentum fluxes opposing those observed in the upper troposphere. It is very unlikely that there are eddy angular momentum fluxes at depth that exactly balance those in the upper troposphere; no model has produced such angular momentum fluxes, and no mechanisms to generate them have been proposed. So the mean zonal winds likely experience dissipation at depth. A plausible dissipation mechanism is the magnetohydrodynamic (MHD) drag that is produced by the interaction of winds with the magnetic field and the Ohmic dissipation of the resulting electric currents. This occurs at depths where the electrical conductivity of the atmosphere is sufficiently large.

The electrical conductivity of hydrogen (Jupiter's main constituent) increases exponentially with depth up to a plateau at  $\sim 0.84R_J$  (Fig. 1a). The electrical conductivity at the plateau ( $2 \times 10^5 \text{ S m}^{-1}$ ) is two orders of magnitude lower than that of a metal conductor (e.g., copper) at room temperature. The Ohmic dissipation produced by the interaction of a given magnetic field with the zonal winds scales linearly with electrical conductivity (Liu 2006; Liu et al. 2008). At  $\sim 0.84R_J$ , zonal winds on the order of  $10^{-2} \text{ m s}^{-1}$  would already experience a substantial dissipation of more than  $1 \text{ W m}^{-2}$  (assuming the magnetic field is of similar strength as in the upper atmosphere; see appendix A). So the zonal winds likely are negligibly weak at this and deeper levels (Liu 2006). Consistent with these inferences, measurements of secular variations of the planetary mag-

netic field indicate that the zonal winds in the electrically conducting interior (inside  $\sim 0.84R_J$ ) are on the order of  $10^{-3} \text{ m s}^{-1}$  (Russell et al. 2001; Guillot et al. 2004). On the other hand, outside  $\sim 0.97R_J$ , the electrical conductivity is so low ( $\lesssim 10^{-3} \text{ S m}^{-1}$ ) that zonal winds of the strength of those observed in the upper troposphere would experience less than  $10^{-2} \text{ W m}^{-2}$  dissipation (about an order of magnitude less than in the simulation in Schneider and Liu (2009)); so substantial zonal winds likely extend to deeper levels. Hence, the Ohmic dissipation produced by interaction with the magnetic field constrains substantial zonal winds to extend to a cutoff radius  $r_c$  that lies somewhere between  $0.84R_J$  and  $0.97R_J$ , corresponding to between about  $1.4 \times 10^6$  and  $3.6 \times 10^4$  bar pressure. Because the electrical conductivity increases exponentially with depth, this constraint on the cutoff radius is not very sensitive to uncertainties about the strength of the magnetic field (which increases with depth, toward the source of the field). For example, a magnetic field an order of magnitude stronger than that at the top of Jupiter's atmosphere would increase the lower bound on  $r_c$  to  $0.89R_J$  (see appendix A).

The Ohmic dissipation constraint derives from the energy balance. Additional constraints derive from the angular momentum and hydrostatic balance. At levels below the cutoff radius, either thermal wind balance has to break down or entropy must be isotropically homogenized, so that the zonal winds can remain weak at these deeper levels. (Otherwise, thermal wind balance and constant entropy gradients perpendicular to the spin axis would continue to imply shear in the direction of the spin axis, implying a reversal and strengthening of zonal winds that would violate the energetic constraints.) Thermal wind balance breaks down where the electrical conductivity is sufficiently large that the dominant balance in the angular momentum equation is no longer geostrophic but the Lorentz force starts to exert a substantial influence on it. Scaling estimates indicate the Lorentz force becomes comparable to the Coriolis force at or below  $\sim 0.94R_J$  (see appendix B). So assuming that radiative fluxes are too weak to isotropically homogenize entropy above  $\sim 0.94R_J$ , it is unlikely that the cutoff radius for substantial zonal winds is larger than that. Therefore, as a conservative bracket for the cutoff radius, we assume it is in the range of  $0.84$  to  $0.94R_J$ , corresponding to 1.4 to 0.2 Mbar pressure.

### c. Possible zonal winds and entropy gradients

Integrating the thermal wind equation (7) along the planet's spin axis from the cylindrical depth  $z_c = z_c(r_c, r_\perp)$  corresponding to the spherical cutoff radius  $r_c$  to the upper troposphere at cylindrical depth  $z_R =$

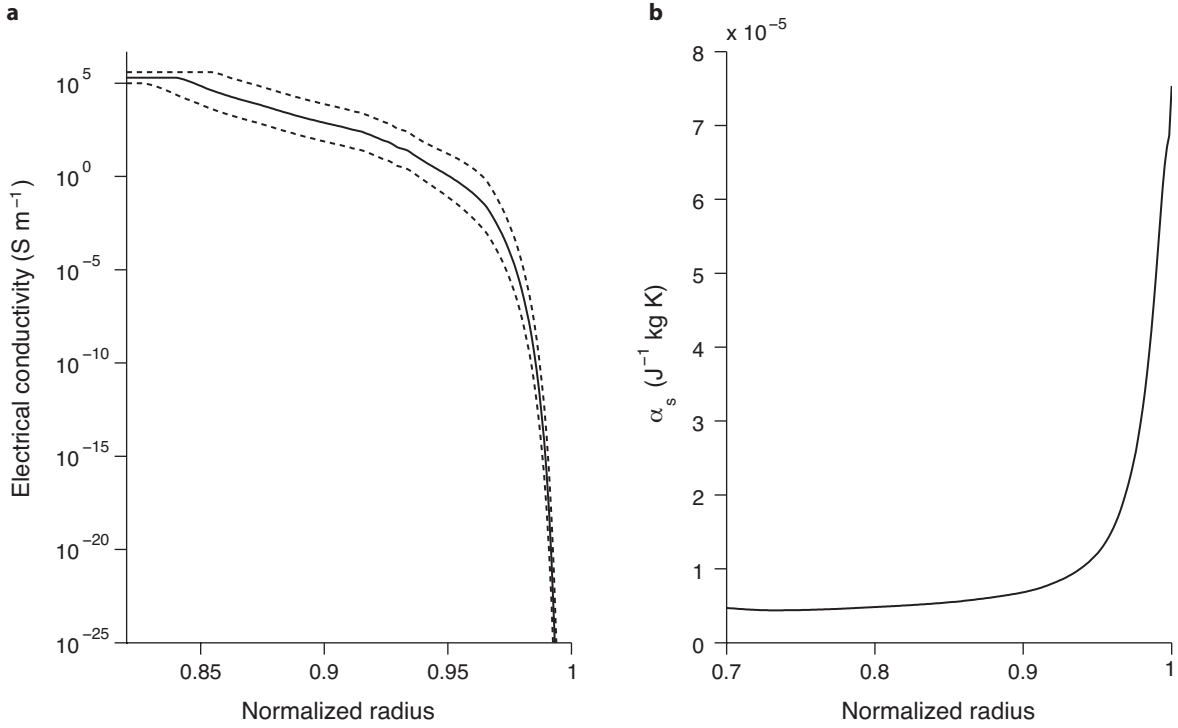


FIGURE 1: (a) Electrical conductivity of hydrogen as a function of normalized radius (solid line) (Nellis et al. 1992, 1996; Liu et al. 2008). Uncertainties from experiments and from the equation of state of hydrogen in Jupiter's interior are indicated by the dashed bounds. Uncertainties owing to heavier elements in the atmosphere are not taken into account. (See Nellis et al. (1992, 1996) and Liu (2006) for further discussion of uncertainties.) (b) Entropic expansion coefficient  $\alpha_s$  as function of normalized radius for the SCVH EOS.

$z_R(R, r_\perp)$  and spherical radius  $R$  gives a relation between the upper-tropospheric zonal wind  $u_R(\phi) = u_R(r_\perp(\phi))$  and the thermal structure of the atmosphere below,

$$u_R(\phi) = \frac{1}{2\Omega} \frac{\partial s'}{\partial r_\perp} \int_{z_c}^{z_R} \alpha_s g \sin \phi' dz. \quad (8)$$

Here,  $\sin \phi' = z/(z^2 + r_\perp^2)^{1/2}$ , and the entropy gradient  $\partial s'/\partial r_\perp$  perpendicular to the spin axis can be taken outside the integral because the assumption that entropy is homogenized along the spin axis implies that the gradient perpendicular to it must be constant going down along the spin axis. Solving for this gradient gives

$$\frac{\partial s'}{\partial r_\perp} = \frac{2\Omega u_R(\phi)}{\int_{z_c}^{z_R} \alpha_s g \sin \phi' dz}, \quad (9)$$

which relates it to the observed upper-tropospheric zonal winds  $u_R$ , the cutoff-radius  $r_c$ , and the entropic expansion coefficient  $\alpha_s$ .

To determine the entropic expansion coefficient  $\alpha_s$ , an equation of state (EOS) is needed. In Jupiter's upper atmosphere, the EOS is well approximated by that for an

ideal gas. Deep in the interior, as the pressure and temperature increase, hydrogen becomes semi-conducting because of the effects of pressure ionization, electron degeneracy, and Coulomb interactions. There, the EOS differs from that for an ideal gas. As in Kaspi et al. (2009), we use the Saumon-Chabrier-Van Horn (SCVH) EOS (Saumon et al. 1995) with the reference entropy measured by the Galileo probe.<sup>2</sup> This adiabatic reference profile matches well with the modeled interior mean density-temperature-pressure profile (Guillot and Morel 1995), although differences exist (Kaspi et al. 2009). In using the SCVH EOS, we ignore the effects of latent heat release in phase transitions (e.g., of water) on the entropy. Figure 1b shows the resulting entropic expansion coefficient  $\alpha_s$  as a function of the normalized radius.

The rapid decrease of  $\alpha_s$  with depth means that, by

<sup>2</sup>The Galileo probe measured an approximately dry adiabatic temperature-pressure profile, passing through 260 K and 4.18 bar (Seiff et al. 1998). Based on the SCVH EOS, the corresponding specific entropy is  $6.27 \times 10^4 \text{ J kg}^{-1} \text{ K}^{-1}$ . The uncertainties about this reference entropy: it may range from 6.24 to  $6.31 \times 10^4 \text{ J kg}^{-1} \text{ K}^{-1}$  (Seiff et al. 1998). But these uncertainties about the reference entropy will only affect the mean entropy, not the meridional entropy gradients and associated temperature gradients that are our focus.

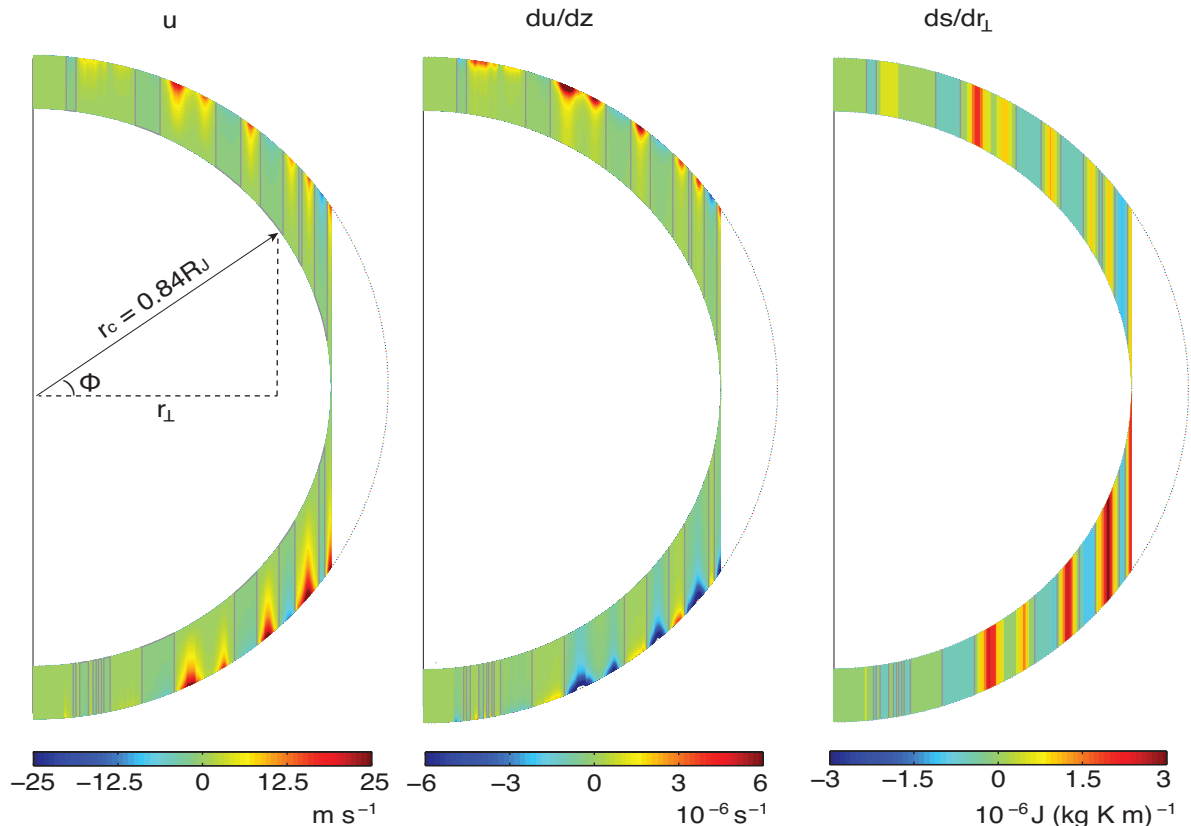


FIGURE 2: Mean zonal wind  $u$  (left), its shear  $\partial u/\partial z$  in the direction of the spin axis (middle), and corresponding entropy gradient perpendicular to the spin axis  $\partial s'/\partial r_{\perp}$  (right), all for a cutoff radius  $r_c = 0.84R_J$ . The gray contours indicate the zero lines.

thermal wind balance (7) and using  $\partial s'/\partial r_{\perp} \approx \text{const}$ , most of the zonal wind shear will be concentrated in the outer few percent of Jupiter's radius, irrespective of where substantial dissipation occurs (see Fig. 2 for an illustration). Thus, the value of the entropy gradient perpendicular to the spin axis (9) is not very sensitive to the chosen cutoff radius, provided it is sufficiently small (cf. Fig. 1b). Whether  $r_c = 0.9R_J$  or to  $r_c = 0.84R_J$  is used changes the integral  $\int_{z_c}^{z_R} \alpha_s g \sin \phi' dz$  by less than 15% when cylinders intersecting midlatitudes in the upper troposphere are considered. The corresponding change in the entropy gradient perpendicular to the spin axis (9) likewise is less than 15%.

These expectations are borne out more precisely by calculations of the entropy gradient perpendicular to the spin axis (9) as a function of  $r_{\perp}$  (expressed as latitude in the upper troposphere) for different cutoff radii  $r_c$  (Fig. 3a). Entropy gradients corresponding to shallowly

confined zonal winds are larger than those corresponding to deeply penetrating zonal winds. Moreover, since  $\alpha_s$  is positive, going downward in the direction of the spin axis (i.e., going toward lower  $|z|$  at fixed  $r_{\perp}$ ), the entropy gradient  $\partial s'/\partial r_{\perp}$  has the same sign as the upper-tropospheric zonal wind. Going downward in the direction of the spin axis where the observed zonal wind is prograde, the entropy gradient  $\partial s'/\partial r_{\perp}$  is positive, so the entropy increases with  $r_{\perp}$ ; the opposite holds where the observed zonal wind is retrograde. The entropy gradient vanishes going downward from where the observed zonal wind vanishes (Fig. 2). Thus, the correlations between the signs of the entropy gradient and of the zonal winds project downward along the spin axis.

In the equatorial region where the cylindrical radius  $r_{\perp}$  is greater than the cutoff radius  $r_c$  (outside the tangent cylinder), the zonal wind shear in the direction of the spin axis and the entropy gradient perpendicular to it

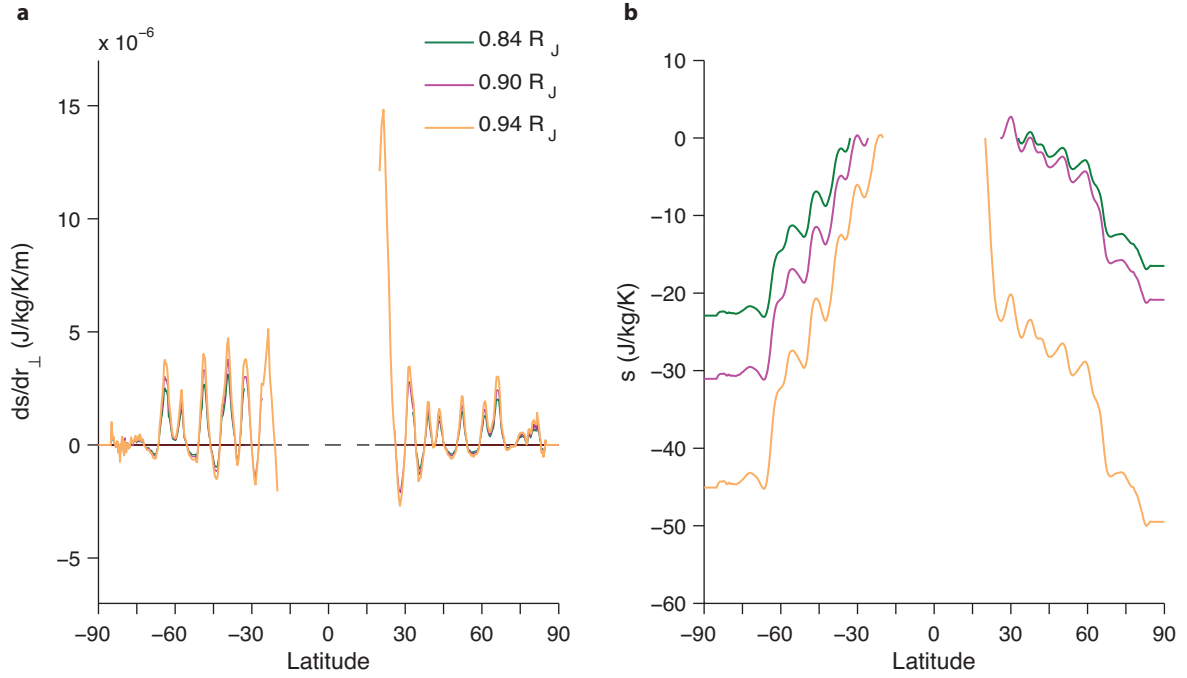


FIGURE 3: (a) Entropy gradient  $\partial s'/\partial r_{\perp}$  perpendicular to the spin axis as a function of latitude  $\phi$  in the upper troposphere. (b) Entropy perturbation (relative to isentropic reference state)  $s'$  as a function of latitude  $\phi$ . Green lines correspond to  $r_c = 0.84R_J$ , magenta lines to  $r_c = 0.90R_J$ , and orange lines to  $r_c = 0.94R_J$ .

are not well constrained by the arguments we presented. Zonal winds within that region still connect with the flow at depth along surfaces of constant angular momentum per unit mass, which are approximately cylinders concentric with the spin axis. But these cylinders no longer intersect a region of substantial MHD drag. The arguments we presented hence do not constrain the zonal wind shear and the entropy gradient in that region (corresponding to latitudes  $|\phi| < \arccos(r_c)$  in the upper troposphere); we have left their values open in Figs. 2 and 3. It is possible that the zonal wind shear in the direction of the spin axis and the entropy gradient perpendicular to it approximately vanish in this region, so that a Taylor-Proudman state is attained (or nearly so).

Where the zonal wind shear and entropy gradients are constrained, the zonal wind can be calculated by integrating the thermal wind balance (7) downward from the observed upper-tropospheric winds. Substituting the expression for the entropy gradient (9) into the thermal wind balance, using  $u(z_c) \approx 0$ , and integrating gives

$$u(z) = u_R(\phi) \frac{\int_{z_c}^z \alpha_s g \sin \phi' dz}{\int_{z_c}^{z_R} \alpha_s g \sin \phi' dz}. \quad (10)$$

This shows explicitly that the zonal winds under our assumptions (principally, that entropy is homogenized in the direction of the spin axis) only depend on the cutoff-

radius  $r_c$  and the EOS, which determines  $\alpha_s$ . It provides a more physical zonal wind structure than those assumed in many previous models.

The zonal winds shown in Fig. 2 are calculated from (10) for  $r_c = 0.84R_J$ . The figure shows that, consistent with the preceding discussion, substantial zonal winds are primarily confined to the upper atmosphere (because of the decrease of  $\alpha_s$  with depth). Generally, the strength both of prograde and retrograde jets decreases with depth toward zero at the cutoff radius  $r_c$ ; zeros of the zonal winds project downward along the spin axis (Schneider and Liu 2009).

#### d. Implications for temperature gradients

To obtain the entropy perturbation  $s'$  in the interior atmosphere as a function of cylindrical radius (or latitude), we integrate equation (9) for the entropy gradient from the pole to the tangent cylinder where  $r_{\perp} = r_c$  (see Fig. 2). As is already clear from the entropy gradients, the equator-to-pole entropy contrast increases with increasing cutoff radius. For  $r_c = 0.84R_J$ , the equator-to-pole entropy contrast is less than  $25 \text{ J kg}^{-1} \text{ K}^{-1}$ ; for  $r_c = 0.94R_J$ , the equator-to-pole entropy contrast is  $50 \text{ J kg}^{-1} \text{ K}^{-1}$ ; for the even larger cutoff radius of  $r_c = 0.9965R_J$  (corresponding to a pressure of 100 bar), which we consider unrealistic, the equator-to-pole en-

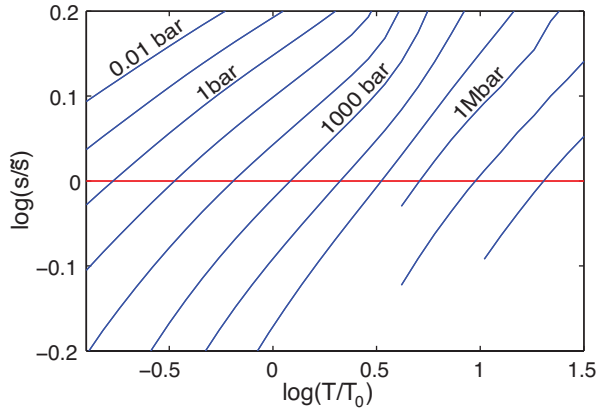


FIGURE 4: Contours of pressure  $p$  as a function of  $\log(s/\bar{s})$  and  $\log(T/T_0)$  for the SCVH EOS (blue). The mean isentropic reference state with the entropy  $\bar{s} = 6.27 \times 10^4 \text{ J kg}^{-1} \text{ K}^{-1}$  determined by Galileo probe measurement at the entry point is shown as the red horizontal line. The reference temperature for normalization is chosen to be  $T_0 = 1000 \text{ K}$ . The first contour in the upper left corner corresponds to  $p = 0.01 \text{ bar}$ , and pressure increases by a factor of 10 for each additional contour to the right.

entropy contrasts would reach  $475 \text{ J kg}^{-1} \text{ K}^{-1}$ . However, these entropy contrasts are still small compared with the entropy of the reference state we assumed ( $\bar{s} = 6.27 \times 10^4 \text{ J kg}^{-1} \text{ K}^{-1}$ , see footnote 2), so the assumption in (1) of small entropy fluctuations about the reference state is well justified.

The temperatures  $T$  corresponding to the entropies  $s$  can be obtained from the EOS. Figure 4 shows contours of pressure  $p$  as a function of  $\log(s/\bar{s})$  and  $\log(T/T_0)$  (reference temperature  $T_0$ ) for the SCVH EOS. The mean temperature increases with pressure in the isentropic reference state, and the magnitude of temperature deviations for a given entropy deviation from the reference state also increases with pressure. For example, a 0.1% deviation of the entropy from the reference state corresponds to a 1.5-K temperature deviation at 1 bar, to a 10-K temperature deviation at  $10^3$  bar, and to a 20-K temperature deviation at  $10^6$  bar.

Figure 5 shows the temperature perturbation as a function of latitude at different pressures and for different cutoff radii. As for the entropy perturbations, the temperature perturbations are larger for shallower cutoff radii. For a cutoff radius of  $0.84R_J$ , the equator-to-pole temperature contrast is  $\sim 0.4 \text{ K}$  at the 1-bar level and  $\sim 1 \text{ K}$  at the 50-bar level. For a cutoff radius of  $0.94R_J$ , the equator-to-pole temperature contrast is  $\sim 0.7 \text{ K}$  at the 1-bar level and  $\sim 2 \text{ K}$  at the 50-bar level. For calculations with unrealistic cutoff radii of  $0.9965R_J$  (corresponding to 100 bar),  $0.9954R_J$  (200 bar), and  $0.9917R_J$

(1000 bar), the temperature contrasts at different pressures are much larger, reaching  $O(10 \text{ K})$  at 50 bar (Fig. 6).

#### e. Implications for Juno's microwave measurements

Juno's microwave instrument is designed to measure the brightness temperature in six channels that are sensitive to different pressure intervals between 0.5 bar and  $O(100 \text{ bar})$ . It is expected to detect relative brightness temperature variations of 0.1%, or variations of 0.1 K in a mean brightness temperature background of 100 K (Janssen et al. 2005).

According to our results, at  $\sim 10$  bar with a mean brightness temperature of 330 K, plausible equator-to-pole temperature contrasts associated with the zonal winds range from  $\sim 0.6 \text{ K}$  (for  $r_c = 0.84R_J$ ) to  $\sim 1.2 \text{ K}$  (for  $r_c = 0.94R_J$ ). These dynamical temperature variations are much larger than the expected detection limit. By contrast, Janssen et al. (2005) shows that a variation in water vapor relative humidity from 100% to 20% has less than 0.1% effect on brightness temperature. Thus, the meridional temperature variations associated with the zonal winds are more easily detectable than variations of water vapor relative humidity.

However, the thermal signals produced by variations of ammonia abundances can be much larger than those produced by the zonal winds. Janssen et al. (2005) shows that increasing the ammonia abundance from 3 to 5 times solar abundance decreases the microwave brightness temperature by 20–25 K. If the ammonia abundances exhibit large meridional variations, it may be difficult to detect the temperature variations associated with the zonal winds. But if ammonia abundances are meridionally homogenized at depth, Juno's microwave measurements, if they indeed will be able to detect relative brightness temperature variations of 0.1%, will provide strong constraints on the cutoff radius of the zonal winds.

### 3. Gravitational signals of deep zonal winds

Written in terms of density rather than entropy, thermal wind balance also gives the density anomalies  $\rho'$  associated with a given zonal wind:

$$\nabla \rho' \times \mathbf{g} = (2\boldsymbol{\Omega} \cdot \nabla) [\tilde{\rho}u]. \quad (11)$$

The azimuthal component, now in spherical coordinates  $(r, \phi)$ , is

$$\frac{\partial \rho'}{\partial \phi} = \frac{2\Omega \cos \phi \tilde{\rho}}{g} \frac{\partial u}{\partial \phi} + \frac{2\Omega r \sin \phi}{g} \frac{\partial \tilde{\rho}u}{\partial r}, \quad (12)$$

where the gravitational acceleration  $g(r)$  continues to be a function of  $r$ . Using the SCVH EOS and assuming a

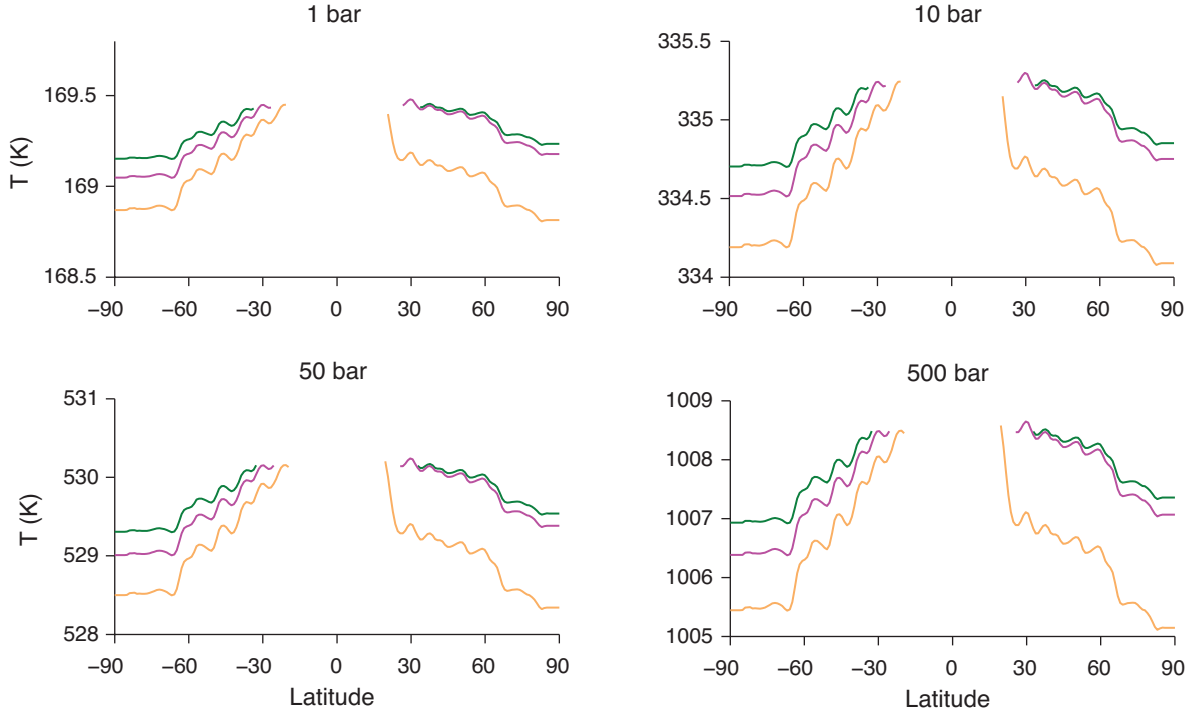


FIGURE 5: Temperature perturbation as a function of latitude at different pressure levels. As in Fig. 3, green lines correspond to  $r_c = 0.84R_J$ , magenta lines to  $r_c = 0.90R_J$ , and orange lines to  $r_c = 0.94R_J$ .

hydrostatic reference state in which the reference density  $\tilde{\rho}$  is only a function of spherical radius  $r$ , we can integrate the thermal wind equation along the meridional direction for any  $r$  and obtain the density perturbation for a given zonal wind distribution (Kaspi et al. 2010).<sup>3</sup>

The density anomaly  $\rho'$  perturbs Jupiter's gravity field through the perturbation of the gravitational potential

$$V(\mathbf{r}) = \frac{GM}{r} \left[ 1 - \sum_{n=2}^{\infty} \left(\frac{a}{r}\right)^n (J_n + \Delta J_n) P_n(\mu) \right]. \quad (13)$$

Here,  $G$  is the gravitational constant,  $M$  is the planetary mass,  $a = R_J$  is the planetary radius (taken at 1 bar),  $J_n$  is the zonal harmonic associated with the hydrostatic reference density distribution  $\tilde{\rho}$  in solid body rotation, and  $\Delta J_n$  is the gravitational zonal harmonic associated

<sup>3</sup>In the calculation of the density perturbation from the thermal wind equation (12), an integration constant  $\rho'_0(r)$  at each spherical radius  $r$  needs to be determined. Although this constant cannot be uniquely determined, we determine  $\rho'_0(r)$  by the requirement that integrated over the sphere with radius  $r$ , the density perturbation vanishes, so that the perturbed state continues to satisfy the hydrostatic balance of the reference state with density  $\tilde{\rho}$ .

with the density perturbation,

$$\Delta J_n = -\frac{1}{Ma^n} \int_0^a r'^{2+n} dr' \int_0^{2\pi} d\phi' \int_{-1}^1 P_n(\mu') \rho' d\mu', \quad (14)$$

where  $\mu' = \sin \phi'$  and  $P_n$  is the Legendre polynomial of degree  $n$ . We consider the gravitational signals produced by hemispherically symmetric zonal winds, which we take to be the winds averaged between the northern and southern hemisphere.

Hemispherically symmetric winds give rise to hemispherically symmetric density perturbations and hence even gravitational zonal harmonics  $\Delta J_n$ ; odd zonal harmonics vanish. In the off-equatorial region, we calculate the winds based on (10), using the observed cloud-level zonal winds averaged between the northern and southern hemisphere as upper boundary condition  $u_R(\phi)$ . In the equatorial region outside the tangent cylinder (outside  $r_{\perp} = r_c$ ), the zonal wind shear in the direction of the spin axis can vanish because cylinders concentric with the spin axis do not intersect the region of MHD drag at depth. We assume the equatorial winds penetrate unabatedly to the interior along the spin axis. As an example, Fig. 7 shows the density anomaly produced by such winds for the cutoff radius  $r_c = 0.84R_J$ . The density anomaly in the equatorial region is greater than

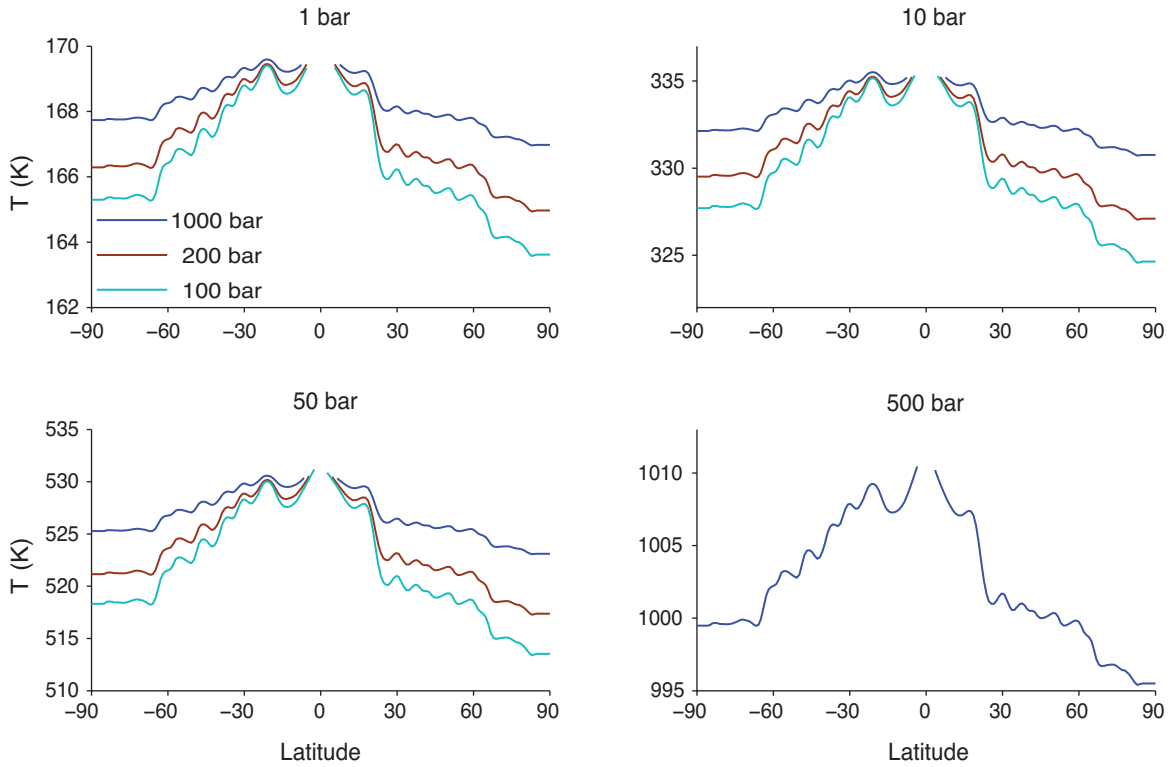


FIGURE 6: Temperature perturbation as a function of latitude at different pressure levels for shallower cutoff radii. Deep blue lines correspond to  $r_c = 0.9917R_J$  (corresponding to 1000 bar), brown lines to  $r_c = 0.9954R_J$  (200 bar), and light blue lines to  $r_c = 0.9965R_J$  (100 bar).

that in the off-equatorial regions because equatorial wind speeds are greater. In the off-equatorial regions, the density anomaly is concentrated in the upper atmosphere due to the concentration of the wind shear there.

The corresponding even gravitational zonal harmonics  $\Delta J_n$  are shown in Fig. 8 for cutoff radii  $r_c = 0.84R_J$ ,  $0.94R_J$ ,  $0.9917R_J$  (corresponding to 1000 bar), and  $0.9965R_J$  (100 bar). For comparison, Fig. 8 also shows the zonal harmonics  $J_n$  of the reference state in solid body rotation, and the zonal harmonics  $\Delta J_n$  for zonal winds decaying very slowly with depth with scale height of  $10^8$  m (Kaspi et al. 2010). The magnitude of the zonal harmonics  $J_n$  of the reference state decreases rapidly with degree  $n$ ; the magnitude of the perturbation zonal harmonics  $\Delta J_n$  associated with zonal winds is smaller for small  $n$  but is sustained for large  $n$ . Thus, to detect the even zonal harmonics associated with zonal winds, Juno's gravity instrument has to detect signals of high degree  $n$ .

The zonal harmonics for deeper cutoff radii ( $0.84R_J$  and  $0.94R_J$ ) are about two orders of magnitude larger than those for a cutoff radius corresponding to 1000 bar, and about three orders of magnitude larger than those for

a cutoff radius corresponding to 100 bar. For zonal winds with cutoff radii of  $0.84R_J$  and  $0.94R_J$ , and for zonal winds that are constant on cylinders (Hubbard 1999), the zonal harmonics  $\Delta J_n$  start to be comparable in magnitude with the zonal harmonics  $J_n$  of the reference state at  $n = 12$ , and they are significantly larger than  $J_n$  for  $n \gtrsim 14$ . For zonal winds with a cutoff radius corresponding to 1000 bar, the zonal harmonics  $\Delta J_n$  start to be comparable in magnitude with  $J_n$  at  $n \gtrsim 14$ ; for even shallower zonal winds, the zonal harmonics  $\Delta J_n$  start to be comparable with  $J_n$  only at even higher  $n \gtrsim 16$ . These results are consistent with those of Kaspi et al. (2010), who found similar relations between the depths of the zonal winds and gravitational zonal harmonics by varying a specified exponential decay depth of the winds.

Juno's gravity instrument is expected to be able to detect gravitational zonal harmonics up to degree 12. It may be able to distinguish cutoff radii of  $0.84$  and  $0.94R_J$  for the zonal winds, and it may distinguish our flow model from zonal winds that are only slowly decaying with depth (Kaspi et al. 2010). Moreover, Juno's gravity instrument can be expected to be able to distinguish deep-flow scenarios (with cutoff radii as shallow as

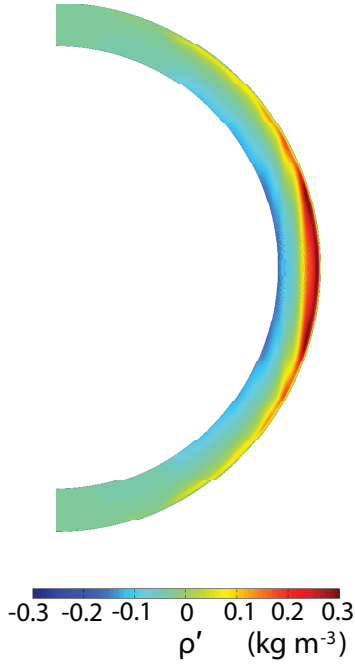


FIGURE 7: Density perturbation  $\rho'$  ( $\text{kg m}^{-3}$ ) for cutoff radius  $r_c = 0.84R_J$ , calculated with the zonal winds averaged between the northern and southern hemisphere.

$0.94R_J$ ) from shallow-flow scenarios (with cutoff radii corresponding to 1000 bar or less), which we consider implausible. If the gravity instrument were not to detect signals from deep zonal winds, the large meridional temperature variations associated with shallow zonal winds and their shear should be detectable by the microwave instrument.

Since the relation (12) between density perturbations and zonal wind perturbations and the decomposition (14) of the gravitational potential into zonal harmonics are linear, the perturbation zonal harmonic  $\Delta J_n$  can be further decomposed into a part associated with equatorial winds and a part associated with off-equatorial winds (inside the tangent cylinder with  $r_\perp = r_c$ ). For deep cutoff radii (such as  $0.84R_J$ ), the gravitational signals produced by equatorial winds dominate (Fig. 9a). For shallower cutoff radii (such as  $0.94R_J$ ), the gravitational signals produced by the off-equatorial winds dominate. Therefore, if the cutoff radius is near the lower end of what we consider plausible, it may be difficult for Juno to detect the gravity signal of deep off-equatorial zonal winds.

#### 4. Conclusions

One of the main goals of the Juno mission is to measure the water and ammonia abundances in Jupiter’s atmosphere below the visible clouds. To achieve this goal, Juno’s microwave instrument is designed to measure the brightness temperature in six different channels sensitive to levels up to  $O(100 \text{ bar})$  (Janssen et al. 2005). However, the thermal signals measured by the microwave instrument come from two different sources: (i) opacity variations produced by variations in the water and ammonia abundances; (ii) temperature variations associated with zonal winds and their shear. Understanding the thermal signals of the zonal winds is crucial for accurately inferring the abundances of water and ammonia. We have shown that there exist strong physical constraints on the structure of the zonal winds, which constrain their thermal as well as gravitational signals.

While it has long been assumed that entropy is completely homogenized in Jupiter’s interior (Guillot et al. 2004), we have argued that convection can only be expected to homogenize entropy along surfaces of constant angular momentum per unit mass, which are approximately cylinders concentric with the spin axis. Entropy gradients perpendicular to these surfaces cannot generally be zero for the flow to satisfy constraints derived from the angular momentum and energy balances. We have used this dynamical constraint on the interior entropy structure together with thermal wind balance to calculate zonal winds and the temperature and density perturbations they imply. To do so, we had to assume a cutoff radius below which zonal winds are negligibly weak. Energetic arguments (that Ohmic dissipation associated with MHD drag at depth can at most be a fraction of the total energy available to drive the flow) and arguments based on the angular momentum balance (that the Lorentz force must be at least comparable to the Coriolis force below the cutoff radius) constrained plausible cutoff radii between  $0.84R_J$  and  $0.94R_J$ .

For the plausible cutoff radii between  $0.84$  and  $0.94R_J$  and using the observed cloud-level winds as upper boundary condition, we calculated the zonal winds and the entropy, temperature, and density perturbations they imply. Because of material properties of hydrogen (its equation of state), strong zonal winds and their shear are concentrated in the outer few percent of Jupiter’s radius, irrespective of the precise value of the cutoff radius. Density variations associated with the zonal winds are also concentrated in Jupiter’s outer layers. As a consequence, gravitational signals associated with zonal winds for different plausible cutoff radii may be difficult to distinguish. However, they are clearly different from gravitational signals associated with zonal winds con-

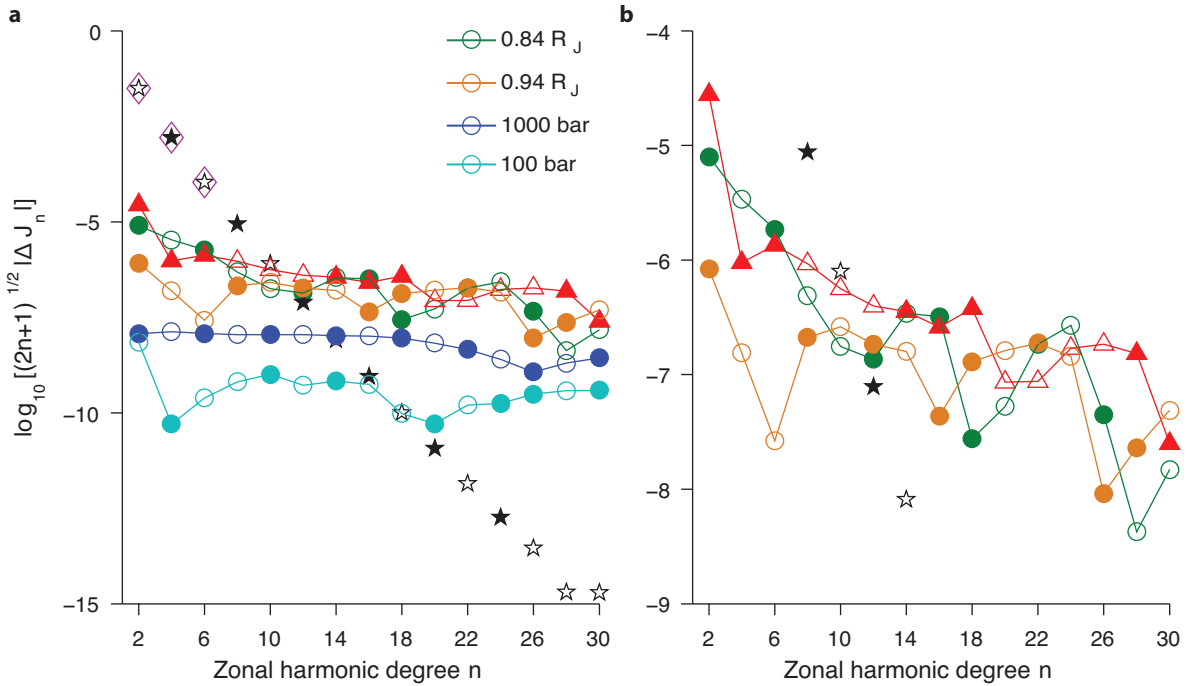


FIGURE 8: Gravitational zonal harmonics associated with hemispherically symmetric zonal winds. (a) Green circles/solid line:  $\Delta J_n$  for  $r_c = 0.84 R_J$ . Orange circles/solid line:  $\Delta J_n$  for  $r_c = 0.94 R_J$ . Deep blue circles/solid line:  $\Delta J_n$  for  $r_c = 0.9917 R_J$  (corresponding to 1000 bar). Light blue circles/solid line:  $\Delta J_n$  for  $r_c = 0.9965 R_J$  (corresponding to 100 bar). For comparison, the red triangles with dash-dotted line show  $\Delta J_n$  for a model with zonal winds slowly decaying with depth with scale height of  $10^8$  m (Kaspi et al. 2010). Black stars shows the gravitational zonal harmonics of the reference state in solid body rotation, and magenta diamonds show observations from Voyager. Juno’s gravity instrument is expected to be sensitive to zonal harmonics up to about degree 12. Filled (open) symbols indicate positive (negative) zonal harmonics. (b) Detailed comparison with enlarged y-axis.

finned above the 1000-bar level. Temperature variations associated with the zonal winds increase with depth. Equator-to-pole temperature contrasts reach  $\sim 1\text{--}2$  K at 50 bar for plausible cutoff radii. This is well above the detection limit of Juno’s microwave instrument, much larger than brightness temperature variations associated with plausible variations in water vapor abundance, but possibly smaller than brightness temperature variations associated with variations in ammonia abundance. Thus, Juno’s gravity instrument can be expected to distinguish deep zonal winds from extremely shallowly confined zonal winds (which we consider implausible), and its microwave instrument can be expected to provide constraints on the cutoff radius of deeper zonal winds provided variations in ammonia abundance can be further constrained by theory and modeling.

As an alternative to our physically based flow model, we have also considered consequences of an alternative scenario, in which zonal winds are confined above the 1000-bar level (outside  $0.9917 R_J$ ). In this case, gravitational signals of the zonal winds would likely not be detectable by Juno, but the equator-to-pole temperature contrasts would reach  $O(10$  K) at 50 bar—a dynamical

temperature signal that would easily be detectable and would likely dominate meridional brightness temperature variations measured by the microwave instrument. So such extreme shallow-flow scenarios should be easily distinguishable from our more plausible deeper-flow scenario.

More generally, our dynamical constraints imply a structure of the zonal winds at depth that derives from a few straightforward and well justifiable assumptions. Calculation of the zonal winds at depth and of the entropy, temperature, and density perturbations they imply does not require a general circulation model, only evaluation of integrals, observations of zonal winds in the upper troposphere, and knowledge of the zeroth-order dynamical balances in the angular momentum equation (geostrophic) and in the radial momentum equation (hydrostatic). This wind structure and the associated temperature and density variations should provide strong constraints for inferring Jupiter’s composition from measurements by the Juno mission.

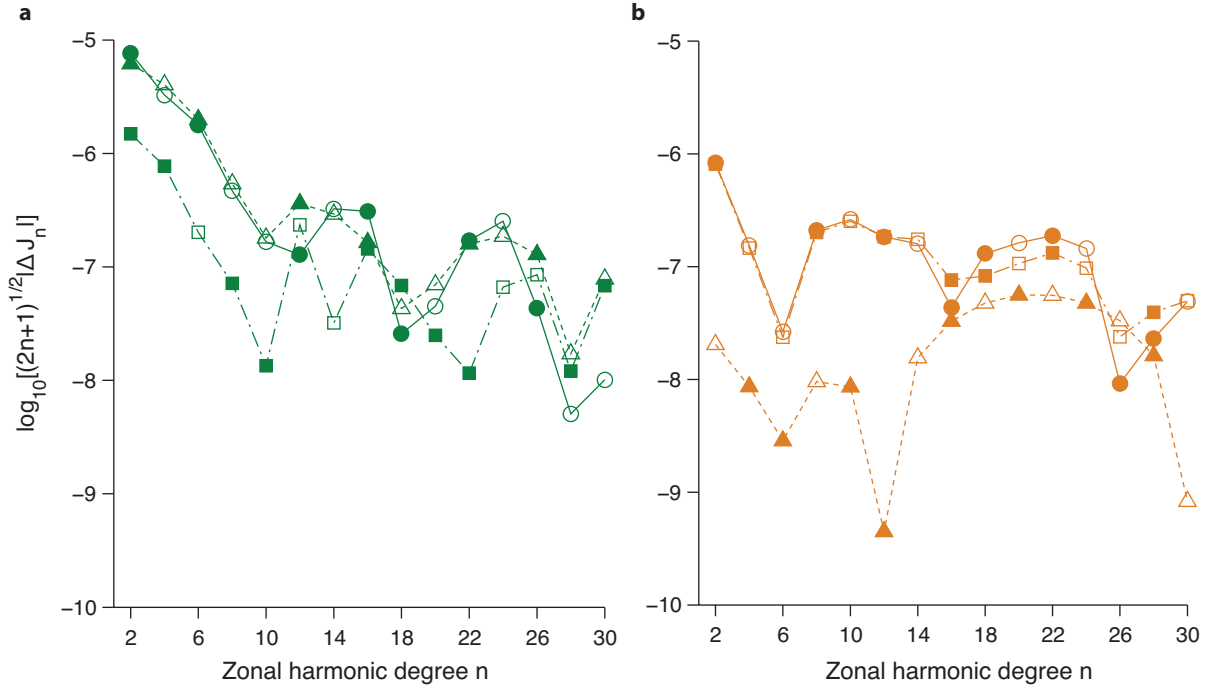


FIGURE 9: Gravitational zonal harmonics associated with hemispherically symmetric equatorial and off-equatorial zonal winds. Circles/solid line: zonal harmonics associated with equatorial and off-equatorial winds. Triangles/dashed line: zonal harmonics associated with equatorial winds. Squares/dash-dotted line: zonal harmonics associated with off-equatorial winds. (a) Cutoff radius  $r_c = 0.84R_J$ . (b) Cutoff radius  $r_c = 0.94R_J$ . Filled (open) symbols indicate positive (negative) zonal harmonics.

## 5. Acknowledgments

This work was supported by a David and Lucile Packard Fellowship and by the NASA Outer Planets Research Program (Grant NNX10AQ05G).

### APPENDIX A

#### Energetic constraints on depth of zonal winds

The Ohmic dissipation per unit volume produced by the interaction of the magnetic field  $\mathbf{B}$  with the flow  $\mathbf{u}$  is given by

$$q = \frac{j^2}{\sigma}, \quad (\text{A1})$$

where  $\sigma$  is the electrical conductivity and  $j$  is the magnitude of the electric current  $\mathbf{j} = \sigma(\mathbf{E} + \mathbf{u} \times \mathbf{B})$ . If we neglect the effect of the electric field  $\mathbf{E}$ , the current scales like  $j \sim UB$  (zonal velocity  $U$  and poloidal magnetic field strength  $B$ ), and the Ohmic dissipation per unit volume can be estimated as

$$q \sim \sigma U^2 B^2. \quad (\text{A2})$$

Because the electrical conductivity is an exponential function of radius (Fig. 1a), the volume-integrated

Ohmic dissipation  $Q$  mainly comes from the deepest layers with substantial zonal winds: a spherical shell extending about a scale height of the electrical conductivity  $H_\sigma$  outward from the cutoff radius  $r_c$ , so that

$$Q \sim 4\pi r_c^2 H_\sigma \sigma U^2 B^2. \quad (\text{A3})$$

Normalizing by the area of the sphere with radius  $R_J$  (to make the Ohmic dissipation directly comparable with the standard intrinsic and solar energy fluxes per unit area in the upper atmosphere), the Ohmic dissipation per unit area is

$$\tilde{Q} \sim H_\sigma \sigma U^2 B^2 \left( \frac{r_c}{R_J} \right)^2. \quad (\text{A4})$$

The magnetic field strength  $B$  entering this dissipation estimate is uncertain. For example, the zonal winds may nonlinearly modify the magnetic field. To evaluate the strength of the magnetic field, we use the dimensionless magnetic Reynolds number  $R_m = UH_\sigma/\lambda$ , where  $U$  is the zonal wind scale,  $H_\sigma$  is the scale height of the electrical conductivity (representing the length scale of field variations), and  $\lambda = (\mu_0\sigma)^{-1}$  is the magnetic diffusivity with magnetic permeability  $\mu_0$ . The magnetic Reynolds number is the ratio of magnetic field generation to magnetic field dissipation. In Jupiter's outer layers where

the electric conductivity of hydrogen is small enough, at depths with  $R_m \lesssim 10$ , the strength of the magnetic field can be estimated by downward continuation of the observed poloidal field in the upper atmosphere. In the deeper interior, at depths with  $R_m \gtrsim 10$ , magnetic field generation through dynamo action is strong and the field can be much stronger than observed in the upper atmosphere. If we take  $U \sim 10 \text{ m s}^{-1}$  and  $H_\sigma \sim 1000 \text{ km}$ , we obtain that  $R_m \sim 10$  when the magnetic diffusivity is  $\sim 1 \times 10^6 \text{ m}^2 \text{ s}^{-1}$ , which occurs around  $0.95R_J$ . Thus, below  $0.95R_J$ , the magnitude of the magnetic field can be significantly greater than the observed outer field.

In the upper atmosphere, the observed poloidal magnetic field is  $B_0 = 4.2 \text{ Gauss}$  (Connerney 1993). If we continue this observed field downward, we have  $B \sim B_0(R_J/r_c)^3$  at the cutoff radius  $r_c$ . For the Ohmic dissipation per unit area, this gives

$$\tilde{Q} \sim H_\sigma \sigma U^2 B_0^2 \left( \frac{R_J}{r_c} \right)^4. \quad (\text{A5})$$

However, the dissipation per unit area is expected to be larger than that given by this estimate at depth where  $R_m \gtrsim 10$  because the downward continuation of the upper-atmospheric field underestimates the magnetic field strength at those depth.

Given the scale height of the electrical conductivity ( $H_\sigma = 1000 \text{ km}$ ) and a zonal velocity  $U$  near the cutoff radius, we can calculate an electrical conductivity  $\sigma(r_c)$  (Fig. 1a) and the associated cutoff radius  $r_c$  at which the Ohmic dissipation per unit area  $\tilde{Q}$  begins to exceed a given threshold dissipation rate. For a threshold Ohmic dissipation of  $\tilde{Q} \sim 1 \text{ W m}^2$  and  $U \sim 10^{-2} \text{ m s}^{-1}$ , this gives the threshold electrical conductivity of  $1.25 \times 10^5 \text{ S m}^{-1}$  and  $r_c \approx 0.84R_J$ . If the magnetic field is an order of magnitude stronger than implied by the downward continuation of the upper-atmospheric field, zonal winds  $U \sim 10^{-2} \text{ m s}^{-1}$  would already experience a substantial dissipation of more than  $\tilde{Q} \sim 1 \text{ W m}^2$  at  $r_c \approx 0.89R_J$ .

## APPENDIX B

### Relative magnitude of Lorentz and Coriolis forces

The Lorentz force can be estimated as

$$F_{\text{Lorentz}} = \sigma (\mathbf{j} \times \mathbf{B}) \sim \sigma (\mathbf{u} \times \mathbf{B}) \times \mathbf{B}, \quad (\text{B1})$$

where the effect of the electric field on the electric current  $\mathbf{j} = \sigma (\mathbf{E} + \mathbf{u} \times \mathbf{B})$  has been neglected. The ratio of the Lorentz and Coriolis forces scales like

$$\frac{|F_{\text{Lorentz}}|}{|F_{\text{Coriolis}}|} \sim \frac{\sigma B^2}{2\Omega\rho}. \quad (\text{B2})$$

If we take  $\Omega \sim 1.76 \times 10^{-4} \text{ s}^{-1}$ ,  $\rho$  as the density in the interior of Jupiter calculated from SCVH EOS (for example,  $\rho \sim 200 \text{ kg m}^{-3}$  at  $0.95R_J$  and  $\rho \sim 600 \text{ kg m}^{-3}$  at  $0.84R_J$ ), and continue the observed magnetic field downward as in appendix A (giving  $B \sim 10 \text{ Gauss}$  at  $0.8R_J$ ), we obtain that the ratio of the Lorentz force to the Coriolis force is about unity at  $0.84R_J$ . If we take the strength of the magnetic field  $B$  below the depths with  $R_m \gtrsim 10$  ( $0.95R_J$ ) to be two orders of magnitude larger than the downward continuation of the observed field (to account for uncertainties in the magnetic field), the ratio of the Lorentz force to the Coriolis force is about unity at  $0.94R_J$ ; it is about an order of magnitude larger inside  $0.91R_J$ . Thus, the depth of  $0.94R_J$  provides a conservative estimate for the upper bound of the cutoff radius.

## REFERENCES

- Atkinson, D. H., A. P. Ingersoll, and A. Seiff, 1997: Deep winds on Jupiter as measured by the Galileo probe. *Nature*, **388**, 649–650.
- Atkinson, D. H., J. B. Pollack, and A. Seiff, 1998: The Galileo probe Doppler wind experiment: Measurement of the deep zonal winds on Jupiter. *J. Geophys. Res.*, **103**, 22 911–22 928.
- Busse, F. H., 1976: A simple model of convection in the Jovian atmosphere. *Icarus*, **29**, 255–260.
- Busse, F. H., 1994: Convection driven zonal flows and vortices in the major planets. *Chaos*, **4**, 123–134.
- Connerney, J. E. P., 1993: Magnetic fields of the outer planets. *J. Geophys. Res.*, **98**, 18 659–18 679.
- Emanuel, K. A., 1983: On assessing local conditional symmetric instability from atmospheric soundings. *Mon. Wea. Rev.*, **111**, 2016–2033.
- Emanuel, K. A., 1994: *Atmospheric Convection*. Oxford University Press, 580 pp.
- Gierasch, P. J., and Coauthors, 2000: Observation of moist convection in Jupiter's atmosphere. *Nature*, **403**, 628–630.
- Guillot, T., 1999: A comparison of the interiors of Jupiter and Saturn. *Planet. Space Sci.*, **47**, 1183–1200.
- Guillot, T., 2005: The interiors of giant planets: Models and outstanding questions. *Ann. Rev. Earth Planet. Sci.*, **33**, 493–530.
- Guillot, T., and P. Morel, 1995: CEPAM: A code for modeling the interiors of giant planets. *Astron. Astrophys. Suppl. Ser.*, **109**, 109–123.
- Guillot, T., D. J. Stevenson, W. B. Hubbard, and D. Saumon, 2004: The interior of Jupiter. F. Bagenal, T. E. Dowling, and W. B. McKinnon, Eds., *Jupiter: The Planet, Satellites and Magnetosphere*, Cambridge University Press, 35–57.
- Hubbard, W. B., 1999: Gravitational signature of Jupiter's deep zonal flow. *Icarus*, **137**, 357–359.
- Ingersoll, A. P., R. F. Beebe, J. L. Mitchell, G. W. Gameau, G. M. Yagi, and J.-P. Müller, 1981: Interaction of eddies and mean zonal flow on Jupiter as inferred from Voyager 1 and 2 images. *J. Geophys. Res.*, **86**, 8733–8743.
- Ingersoll, A. P., and Coauthors, 2004: Dynamics of Jupiter's atmosphere. F. Bagenal, T. E. Dowling, and W. B. McKinnon, Eds., *Jupiter: The Planet, Satellites and Magnetosphere*, Cambridge University Press, 105–128.
- Janssen, M. A., M. D. Hofstadter, G. S., A. Ingersoll, M. Allison, S. J. Bolton, S. M. Levin, and L. W. Kamp, 2005: Microwave remote sensing of Jupiter's atmosphere from an orbiting spacecraft. *Icarus*, **173**, 447–453.
- Kaspi, Y., G. R. Flierl, and A. P. Showman, 2009: The deep wind structure of the giant planets: results from an anelastic general circulation model. *Icarus*, **202**, 525–542.
- Kaspi, Y., W. Hubbard, A. P. Showman, and G. R. Flierl, 2010: Gravitational signature of Jupiter's internal dynamics. *Geophys. Res. Lett.*, **37**, L01 204.

- Liu, J. J., 2006: *Interaction of the magnetic field and flow in the outer shells of giant planets*. Caltech Thesis, 165 pp.
- Liu, J. J., P. M. Goldreich, and D. J. Stevenson, 2008: Constraints on deep-seated zonal winds inside Jupiter and Saturn. *Icarus*, **196**, 653–664.
- Liu, J. J., and T. Schneider, 2010: Mechanisms of jet formation on giant planets. *J. Atmos. Sci.*, **67**, 3652–3672. Giant planets.
- Magalhães, J. A., A. Seiff, and R. E. Young, 2002: The stratification of Jupiter's troposphere at the Galileo probe entry site. *Icarus*, **158**, 410–433.
- Nellis, W. J., A. C. Mitchell, P. McCandless, D. J. Erskine, and S. T. Weir, 1992: Electronic energy gap of molecular hydrogen from electrical conductivity measurements at high shock pressures. *Phys. Rev. Lett.*, **68**, 2937–2940.
- Nellis, W. J., S. T. Weir, and A. C. Mitchell, 1996: Metallization and electrical conductivity of hydrogen in Jupiter. *Science*, **273**, 936–938.
- Porco, C. C., and Coauthors, 2003: Cassini imaging of Jupiter's atmosphere, satellites, and rings. *Science*, **299**, 1541–1547.
- Russell, C. T., Z. J. Yu, and M. G. Kivelson, 2001: The rotation period of Jupiter. *Geophys. Res. Lett.*, **28**, 1911–1912.
- Salyk, C., A. P. Ingersoll, J. Lorre, A. Vasavada, and A. D. Del Genio, 2006: Interaction between eddies and mean flow in Jupiter's atmosphere: Analysis of Cassini imaging data. *Icarus*, **185**, 430–442.
- Sánchez-Lavega, A., and Coauthors, 2008: Depth of a strong Jovian jet from a planetary-scale disturbance driven by storms. *Nature*, **451**, 437–440.
- Saumon, D., G. Chabrier, and H. Van Horn, 1995: An equation of state for low-mass stars and giant planets. *Astrophys. J.*, **99**, 713–741.
- Schneider, T., and J. Liu, 2009: Formation of jets and equatorial superrotation on Jupiter. *J. Atmos. Sci.*, **66**, 579–601.
- Seiff, A., and Coauthors, 1998: Thermal structure of Jupiter's atmosphere near the edge of a 5- $\mu\text{m}$  hot spot in the north equatorial belt. *J. Geophys. Res.*, **103**, 22 857–22 889.
- Thorpe, A. J., and R. Rotunno, 1989: Nonlinear aspects of symmetric instability. *J. Atmos. Sci.*, **46**, 1285–1299.